Imaging microspectroscopy of Ni/Fe/Co/Cu(001) using a photoemission microscope

W. Kuch[a,*], J. Gilles[a], F. Offi[a], S.S. Kang[a], S. Imada[b], S. Suga[b], J. Kirschner[a]

[a]*Max-Planck-Institut für Mikrostrukturphysik, Weinberg 2, D-06120 Halle, Germany*
[b]*Graduate School of Engineering Science, Osaka University, 1–3 Machikaneyama, Toyonaka 560-8531, Japan*

Abstract

The magnetic phases of 0–6 atomic monolayers (ML) Ni/0–14 ML Fe/6 ML Co/Cu(001) trilayer crossed double wedges are studied by the combination of photoelectron emission microscopy and X-ray magnetic circular dichroism spectroscopy at the Fe $L_{2,3}$ edges. This microspectroscopic technique allows the extraction of local quantitative magnetic information. The presence of three magnetically different thickness regions of Fe with effective spin moments per atom of 2.5 μ_B (below ≈ 3.5 ML), 0.7 μ_B (≈ 3.5–11 ML), and 2.0 μ_B (above ≈ 11 ML) is confirmed. At 7–9 ML thickness, the value of 0.7 μ_B is consistent with a ferromagnetic Fe surface layer on top of non-ferromagnetic layers. The ratio of orbital to effective spin moment varies between 0.05 for very thin Fe films and 0.15 for thicker films, if correction of saturation effects is taken into account. Images of the magnetic circular dichroism asymmetry at the Ni and Co L_3 edges show that at 5.5 ML Fe thickness the Ni and Co magnetizations have opposite orientations, pointing towards antiferromagnetic coupling across the Fe layer. © 2000 Elsevier Science B.V. All rights reserved.

Keywords: Photoelectron emission microscopy; X-ray magnetic circular dichroism; Fcc Fe; Thin films; Magnetic moment

1. Introduction

Since its experimental discovery [1], magnetic circular dichroism in soft X-ray absorption (XMCD) spectroscopy has developed into a widely used technique for the element-specific characterization of magnetic thin films and multilayers [2,3]. The absorption of circularly polarized photons at elemental absorption edges differs for different alignment of light helicity and magnetization direction [4], leading to a difference in secondary electron intensity. Sum-rules have been proposed to deduce quantitative information from the difference curve between absorption spectra for opposite light helicity [5,6]. Although there has been some dispute about the applicability of these rules [2,7–11], they seem to yield reasonable results for the 3*d* transition metals [2,3,10,12–15]. These sum-rules allow one to extract numbers for the spin and orbital magnetic moments from the comparison of the integrated absorption cross section at the L_3 and L_2 edges of transition metals for opposite light helicity, thereby enabling the separate determination of magnetic properties of different elements in the same sample.

The rapidly decreasing size of technologically employed magnetic structures calls for techniques

*Corresponding author. Tel.: +49-30-6392-4927; fax: +49-30-6392-4984.
E-mail address: kuch@exp.bessy.de (W. Kuch).

that allow quantitative magnetic characterization on a microscopic scale. One way to add spatial resolution to the advantages of magnetic circular dichroism spectroscopy is the use of a photoelectron emission microscope (PEEM). In PEEM imaging, the lateral intensity distribution of emitted low energy secondary electrons is magnified by an electron optics. The intensity of secondary electrons can be used as a surface sensitive measure of the absorption of soft X-rays. It is therefore straightforward to combine the principles of microscopy (PEEM) and spectroscopy (XMCD) in order to unite the advantages of both methods, namely the element-selective quantitative information of electronic and magnetic properties of XMCD, and the lateral resolution of PEEM. This is called microspectroscopy, and can supply images displaying local electronic and magnetic properties of a sample as determined from the analysis of local XMCD spectra.

The effect of XMCD, i.e., the dependence of the absorption of circularly polarized photons at elemental absorption edges on the alignment of the magnetization direction and the light helicity, has in fact been employed as a contrast mechanism for the imaging of magnetic domains with PEEM [16–19]. Domains on the sample that have different geometrical projections of the magnetization direction onto the direction of the incoming X-rays show a different absorption cross section for circularly polarized photons at the absorption resonance. Imaged with PEEM, these domains can be distinguished by their different intensity of secondary electron emission. To obtain furthermore the *full* spectroscopic information inherent to XMCD requires the recording of microscopic images of the secondary electron intensity at many different photon energies for both helicities, not only at the absorption maximum. These images then constitute a set of local XMCD spectra for any position of the imaged sample area. Standard sum-rule analysis may then be performed for all pixels constituting the image in order to obtain images showing the absolute numbers of the components of spin and orbital magnetic moments along the light direction. The acquisition of such a spectral series of absorption images, or, in other words, the parallel recording of local XMCD spectra in a reasonable time became feasible with the availability of powerful third generation synchrotron light sources.

In this contribution we use PEEM–XMCD microspectroscopy to investigate the magnetic phases and the coupling behavior of ultrathin Fe films sandwiched between Ni and Co films on Cu(001). A common means of effectively studying the thickness dependence of thin film properties is to image their spatial distribution in wedge-shaped samples. The two-dimensional information present in plane images can be used to study the dependence of these properties on two independent parameters, for example the thicknesses of two of the constituting films. For the present study we prepared Ni/Fe/Co/ Cu(001) films in which the Co thickness was constant at 6 atomic monolayers (ML), and in which both the Fe and the Ni layer were deposited as wedges, rotated by 90° in the film plane with respect to each other. To be able to image such wedge-shaped samples with PEEM, microscopic dimension wedges of 255-μm size were used.

Ultrathin epitaxial Fe films, grown at room temperature on Cu(001), are one of the most interesting systems with respect to the interplay between structural and magnetic properties [20–38]. For film thicknesses below ≈ 4 atomic monolayers (ML) a fully ferromagnetic tetragonally expanded fcc-like structure is present [20,21]. In the thickness range between 4 and 11 ML, a second phase with a relaxed fcc structure is found, in which one observes a non-ferromagnetic behavior of the inner film layers and ferromagnetism at the surface [22–25]. For thicknesses above ≈ 11 ML appears a third phase, a ferromagnetic (011) oriented bcc phase [26–28]. Fe films grown on Co/Cu(001) exhibit a very similar sequence of structural and magnetic phases [39–44]. The main difference with respect to Fe/Cu(001) concerns the direction of the easy magnetic axis in phases I and II, which is out-of-plane in the case of Fe/Cu(001) [29–32], and in-plane for Fe/Co/ Cu(001). As for the presence of the ferromagnetic surface layer in the second phase, controversial experimental evidence has been reported. While from oxygen adsorption [41,42] and XMCD experiments [39,40] it has been concluded that the surface is not ferromagnetic, other XMCD measurements [43] as well as measurements of photoelectron diffraction in magnetic dichroism [45] and spin-resolved valence band photoemission [46] provided evidence for the presence of a ferromagnetic surface layer on top of

non-ferromagnetic underlayers. Our own previous PEEM–XMCD microspectroscopy experiments of Fe/Co/Cu(001) gave a spin moment of ≈ 0.7 μ_B in the second phase, which also supports the conclusion of a ferromagnetic Fe surface [44].

In Fe/Ni$_{81}$Fe$_{19}$ multilayers, it has been observed that non-ferromagnetic fcc Fe layers similar to the ones that exist in the second phase of Fe/Cu(001) or Fe/Co/Cu(001) can give rise to an antiferromagnetic coupling between the Ni$_{81}$Fe$_{19}$ layers at certain Fe layer thicknesses [47]. Using the magneto-optic Kerr effect, Escorcia-Aparicio et al. found that Co/Fe/Co/Cu(001) films could not be saturated around 8 Å Fe film thickness in 1.9 kOe magnetic fields, which is a hint towards antiferromagnetic coupling of the two Co layers [41,42]. Except for Refs. [41,42] no other reports concerning antiferromagnetic interlayer coupling across fcc Fe films on Cu(001) substrates came to our knowledge. In this contribution, we study Ni/Fe/Co trilayers, in which the Ni and Fe layers are deposited as crossed wedges. This allows the imaging of the dependence of the magnetic properties on the thickness of both Ni and Fe layers. The use of Ni instead of Co as the top magnetic layer has the advantage that the magnetic signal of each layer, Co, Fe, and Ni, can be determined separately by virtue of the element-selectivity of XMCD, allowing the layer resolved characterization of the entire system. By imaging the onset of the Ni wedge, it is possible to compare the uncovered Fe/Co film with the Ni/Fe/Co trilayer. We find, indeed, that in the Ni/Fe/Co trilayers, antiferromagnetic coupling of the Ni and Co layers across the non-ferromagnetic Fe occurs at an Fe layer thickness of about 5.5 ML. In the Fe/Co bilayers, on the other hand, no indication for antiferromagnetic alignment between the Co magnetic layer and the Fe surface layer could be observed.

2. Experimental

The experiments were performed at room temperature in an ultrahigh vacuum chamber (base pressure 1×10^{-8} Pa in the sample preparation chamber, and 2×10^{-8} Pa in the PEEM chamber) equipped with standard facilities for sample preparation and surface characterization. Co, Ni, and Fe films were evapo-

rated at room temperature by electron bombardment of high purity rods. Deposition rates were about 0.4 ML/min for Co and Ni, and 0.6 ML/min for Fe. The evaporation rates were calibrated before preparation of the wedges for continuous films evaporated under identical conditions by means of the oscillations in medium energy electron diffraction intensity recorded during the growth. The accuracy of the film thicknesses cited here is estimated as 10%. The wedge-shaped films were prepared by placing an aperture of 2×0.5 mm^2 in front of the sample, with a distance to the sample surface of 1 mm. During deposition, the sample was rocked by $\pm 7.5°$ about the long axis of the aperture, which was set at a 90° different sample azimuth for Fe and Ni deposition. The total evaporation time corresponded to 6 ML for Co and Ni, and 14 ML for Fe. This results in four 255×255 μm^2 regions of crossed wedges with slopes of 0.055 and 0.023 ML/μm for Fe and Ni, respectively. A sketch of the crossed wedges is shown in Fig. 1. The circle highlights the approximate region in which the measurements were carried out. The samples were magnetized after the deposition of the continuous Co film by a field of 500 Oe along the [110] direction of the Cu substrate, and again immediately before the measurements in the photoemission microscope by a pulsed field of 310 Oe.

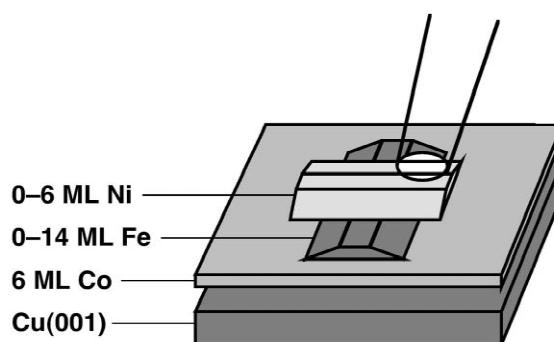Synchrotron radiation from the twin helical undulator beamline for soft X-ray spectroscopy

Fig. 1. Sketch of the sample. The wedge-shaped Fe and Ni films were prepared by evaporation through apertures of 2×0.5 mm^2 placed 1 mm in front of the sample, and rocking the sample about the long axis of the aperture. The circle highlights one of the four areas of crossed Ni–Fe double wedges in which the measurements were carried out.

BL25SU of SPring-8 in Japan was used. Circularly polarized light emitted in the first harmonic from one of two undulators is monochromatized by a varied spacing plane grating monochromator [48]. After having set the two undulators to opposite helicity, helicity reversal was realized by closing one undulator and fully opening the other, which took about 10 min. The degree of circular polarization is >98%. The light was incident to the sample under a grazing angle of 30° from the surface, with an azimuthal angle of 18° to the [110] axis of the Cu substrate. The entrance and exit slits of the monochromator were set to 290 μm for the measurements presented here. Since the light spot on the sample is an image of the exit slit, the local energy resolution at a certain spot on the sample does not depend on the slit size. It is estimated to be better than 150 meV, so that the spectra can be regarded as representing mainly the intrinsic lineshape of the Fe $L_{2,3}$ absorption edges. All images were normalized to the electron current measured at the last optical element, a gold-coated refocusing mirror. In order to minimize deviations in the ratio between the integral photon flux measured in that way and the local flux density in the imaged area, apertures behind the exit slit of the monochromator were adjusted to reduce the excess illuminated area at the sample surface outside the field of view of the microscope

The set-up of the photoemission microscope (Focus IS-PEEM; FOCUS GmbH, Hünstetten, Germany) is identical to that described in previous publications [17–19]. In short, it consists of a three-lens electrostatic straight optical axis microscope with an integral sample stage and a variable contrast aperture. To obtain a large field of view, a low extraction voltage of about 200 V was used. This results in a lateral resolution of about 1 μm and a field of view of about 380 μm. The magnified image is intensified by a two-stage microchannel plate, and converted into visible light by means of a scintillator crystal. The image is then computer-recorded with 12-bit resolution by a Peltier-cooled camera (PCO SensiCam; PCO Computer Optics GmbH, Kelheim, Germany). An 8×8 binning of camera pixels was used for the images presented here. One pixel then corresponded to 3×3 μm^2 of the sample surface. To reduce the amount of data, the region of interest was limited to a rectangle of 100×76 pixels, or $300 \times$

228 μm^2. The exposure time per image was 10 s. A total of 121 images for each helicity were recorded as a function of photon energy in the interval between 701 and 728 eV. The helicity was reversed only once after completion of a full energy scan. The total acquisition time was about 1 h 15 min, which included the moving time of the monochromator for wavelength scanning and the time needed to reverse the helicity.

3. Data analysis

For the computerized automatic sum-rule analysis of all of the 7600 XMCD spectra, a template spectrum fit similar to that described in more detail in Ref. [49] was used. Before fitting the single pixel data, a correction concerning deviations between the local photon flux at the position of each pixel and the integral photon flux from the mirror current caused by the angular distribution of the intensity in the undulator radiation had to be performed. After normalizing all images to the mirror current, images taken with light from the downstream undulator, which was set to deliver light of positive helicity, were scaled down by a factor that depended linearly on energy. This energy dependent correction factor was determined from fitting a straight line to the ratio of two absorption spectra for opposite helicity after normalization, thereby excluding the peak regions from the fit in which the dichroism occurs. This was done separately for all pixels in the image. The correction determined in that way did not exceed 5%. The spectra were then normalized to unity edge jump by adjusting the intensity axes of the spectra to zero in the pre-edge region, and to one in the post-edge region.

A template XMCD spectrum for the fits was obtained from summing up the spectra of 5644 pixels over the full range of the Fe wedge for Ni thicknesses from 0 to 3.5 ML. The sum-rule analysis of the template curve was done as in Refs. [50,51], thereby following the procedure described in Refs. [2,3]. In particular, a background consisting of two step functions of 0.5 eV width and relative statistical heights of 2/3 and 1/3 at the positions of the L_3 and L_2 absorption maxima, respectively, was subtracted from the spectra in order to obtain the white line

intensity. We assumed that the resulting integral of the helicity-averaged absorption spectra corresponded to 3.34 Fe 3d holes [7]. The difference between the absorption spectra for opposite light helicity were corrected for the angle of incidence with respect to the [110] magnetization direction, and for the degree of light polarization, which was taken as 98%. Evaluating the Fe spin and orbital magnetic moments by applying the sum rules [5,6] to the integral of the difference spectrum of measurements with opposite helicity, and normalizing to the white line intensity gives then an effective spin magnetic moment of the template spectrum $\mu_{S,eff} = (1.09\pm0.06)$ μ_B and an orbital magnetic moment $\mu_L = (0.28\pm0.06)$ μ_B. The effective spin magnetic moment is the quantity that is obtained from the application of the spin sum rule [6], and includes besides the spin magnetic moment μ_S also a contribution from the magnetic dipole term $\frac{7}{2}T_z$. The latter is zero in the bulk of cubic crystals, but can be of the same magnitude as the orbital moment in ultrathin films [52–56]. The above values represent a spatial average over the imaged area of the Ni/Fe double wedge, weighted by the local intensity. The errors quoted here represent the accuracy of the data. An additional systematic error that can be up to 20% may be present due to the details of background subtraction, the number of 3d holes, saturation effects [15,57–59], the degree of circular polarization, or the overlap between $2p_{3/2}$ and $2p_{1/2}$ final states [11].

We have to consider that the energy scans presented here were taken only up to an energy of 728 eV in order to keep data acquisition times short, and to avoid contamination of the surface. Part of the tail of the L_2 dichroism at higher photon energies is therefore not included in the analysis. This leads to systematic deviations of the magnetic moments as determined by the sum-rules, predominantly of the orbital moment. A cut-off in the integration on the high energy side of the spectra leads to a higher apparent orbital moment [60]. To quantify this effect we have re-analyzed the bulk Fe data of Ref. [2] after cutting off the high photon energy tail at 728 eV in the same way we analyzed our own data, in particular, after applying the local flux correction procedure described above. From that we obtained an orbital moment which is a factor of 2.6 ± 0.2

higher, whereas the effective spin moment is affected by less than 5%. To account for that, we corrected our orbital moments' values by a factor of 1/2.6. The template curve orbital moment is thus $\mu_L = (0.11\pm0.02)$ μ_B. The reason for the stronger correction of the orbital moment is that the small missing dichroism signal from the high energy tail has a relatively higher influence on the smaller orbital moment, which is calculated from the difference of the L_3 and L_2 dichroism, than on the larger spin moment, where they are summed. As will be seen in Section 5, the corrected values of the Fe orbital moments are in reasonable agreement with values from literature, whereas without the correction the quantitative agreement would be lacking.

The pixel-by-pixel analysis could be done afterwards by fitting that template difference curve separately to all of the single pixel difference curves. Only two parameters were used for that, which describe the individual scaling of the difference curve in the L_3 and L_2 regions. The white line intensity was assumed to be proportional to the helicity averaged L_3 peak height. Only a smooth spatial variation of the white line intensity of less than 20% was present in the spectra over the full imaged area. Sum-rule analysis of the single pixel data is obtained from the two fit parameters, based on the analysis of the template spectra. The two degrees of freedom of the fit to the template curve are thus easily converted into numbers for the Fe spin and orbital moment for every pixel in the image. By using only two-fit parameters connected to the dichroism intensity at the L_3 and L_2 edge, the fit procedure is very stable, which is a prerequisite for obtaining meaningful information from noisy or scattered single pixel data. This analysis is valid if the shape of the absorption spectra does not change over the imaged area. This was checked to be the case for the Fe spectra presented here.

To illustrate the template fit procedure, three typical single pixel XMCD spectra from 3×3 μm^2 areas of the sample surface are shown in Fig. 2. The pixels denoted (a), (b), and (c) correspond to Fe thicknesses of ≈ 2, 5, and 10 ML, respectively, capped by ≈ 1.2 ML Ni. These pixels have been chosen to show strongly different Fe magnetic moments; the Fe thickness of (a) corresponds to phase I, that of (b) to phase II, and that of (c) to the
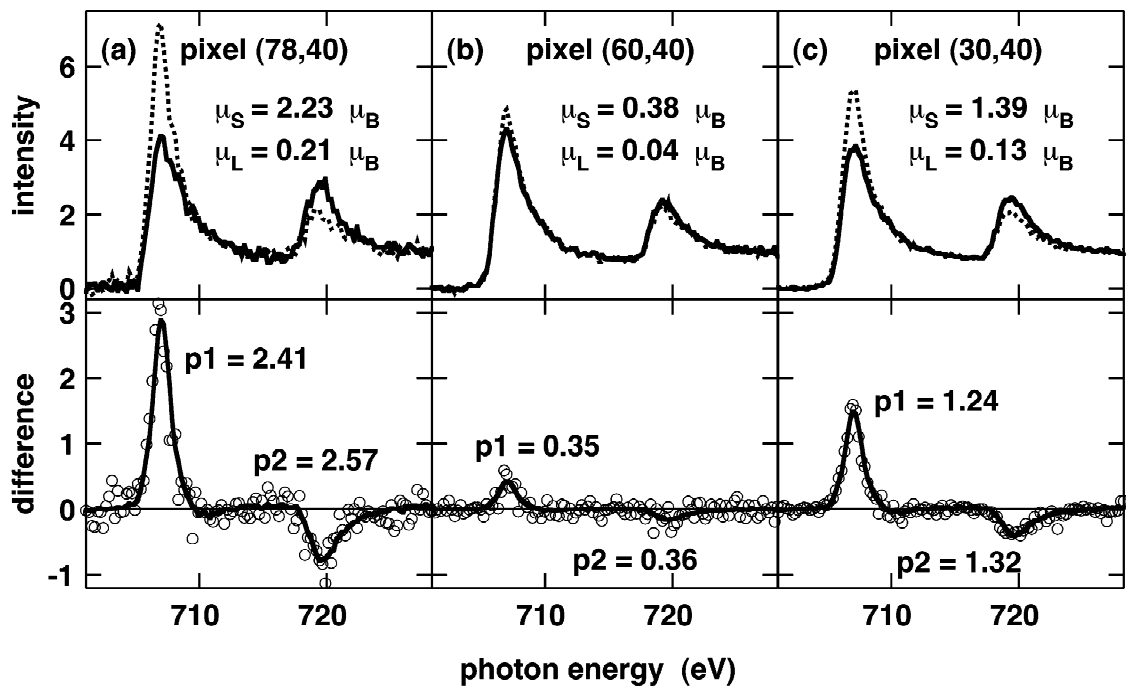
Fig. 2. Single pixel XMCD spectra from three different 3×3 μm^2 spots on the sample surface. (a) Data of pixel (78,40) ($x - y$ coordinates (234, 120 μm), ≈ 2 ML Fe thickness), (b) data of pixel (60,40) ($x - y$ coordinates (180, 120 μm), ≈ 5 ML Fe thickness), (c) data of pixel (30,40) ($x - y$ coordinates (90, 120 μm), ≈ 10 ML Fe thickness). Top: single pixel absorption spectra for positive (dotted lines) and negative helicity (solid lines). Bottom: corresponding difference curves (solid symbols) and fit using a template difference spectrum (lines), scaled by the fit parameter p_1 (p_2) at the L_3 (L_2) edge, as indicated, in order to fit the respective single-pixel difference curves. The results of the fits in terms of spin and orbital moments are given in the top panel. Note the different vertical scale in the top and bottom panels.

transition region between phases II and III. In the top panel, the absorption spectra of each of the three pixels for positive and negative helicity are reproduced as dotted and solid lines, respectively. The corresponding dichroism curves are shown underneath as the difference between these two curves (solid symbols). The lines in the difference spectra represent the template difference spectrum, scaled by the fit parameters $p1$ at the L_3 edge, and $p2$ at the L_2 edge to fit the respective single pixel difference data. The results of the fits for these pixels in terms of spin and orbital moments are given in the top panel. Note how the noise, as seen from the scatter in the difference data, is reduced for thicker Fe films.

4. Results

The result of the pixel-by-pixel sum-rule analysis for the Fe effective spin moment $\mu_{S,eff}$ is presented

in Fig. 3a. Different levels of gray correspond to different values of $\mu_{S,eff}$, as explained in the legend on the left hand side. The Fe and Ni thicknesses of the crossed double wedge are given at the top and right axes, respectively. The behavior of the Fe spin moment in the crossed double wedge is dominated by a strong dependence on the Fe film thickness. Three different regions labeled I, II, and III in Fig. 3 at approximately 0–3.5 ML, 3.5–11 ML, and >11 ML Fe thickness are clearly recognized by their different moments. They can be correlated to the three different magnetic phases of Fe, as outlined in Section 1. A black stripe indicating a strongly reduced Fe spin moment is recognized around 5.5 ML Fe thickness and Ni coverages of more than 1.5 ML. Another effect of the Ni cap layer seems to be a small shift of the transition from phase I to phase II towards lower Fe thicknesses starting just at the onset of the Ni wedge. The reduced moment in the upper right corner at Fe thicknesses below 2 ML, in
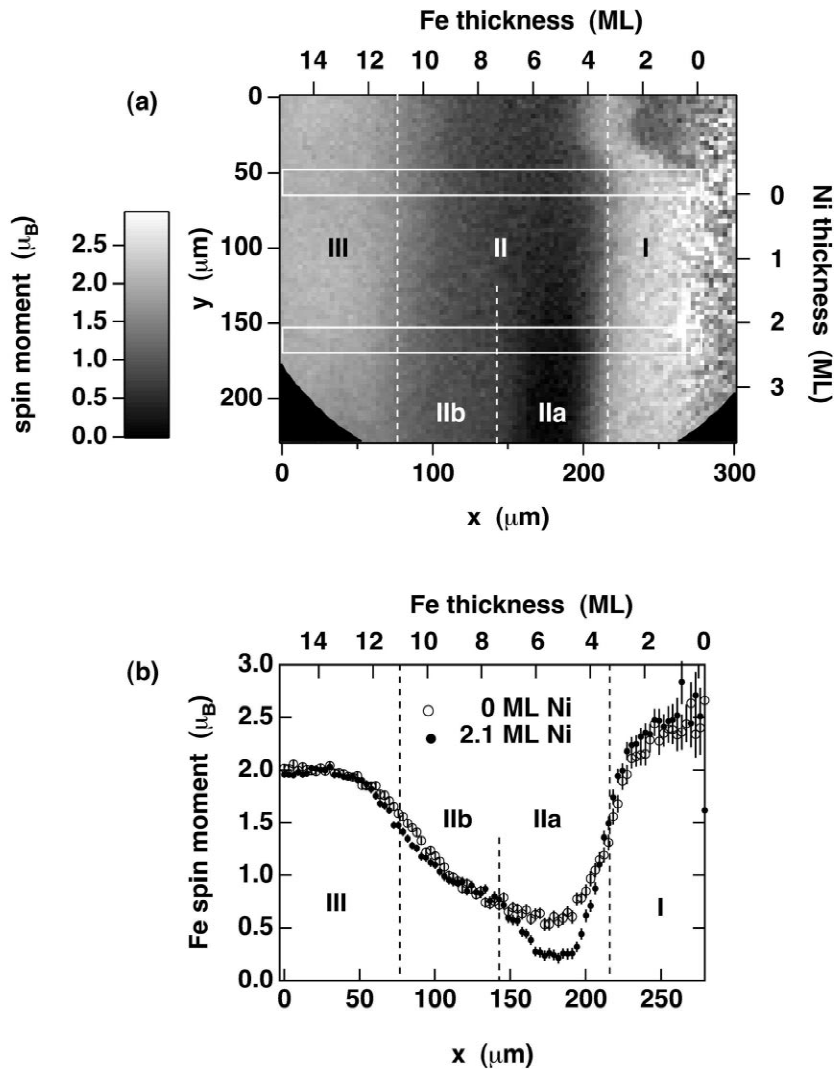
Fig. 3. (a) Result of the pixel-by-pixel sum-rule analysis for the Fe effective spin moment $\mu_{S,eff}$. Different levels of gray correspond to different values of $\mu_{S,eff}$, as explained in the legend. The thickness of the Fe wedge increases from right to left, the thickness of the Ni wedge from top to bottom, as indicated at the top and right axes. Regions with different values of $\mu_{S,eff}$ are separated by dashed vertical lines and labeled I through III, IIa, IIb. The white rectangles indicate the positions at which linescans are presented in panel (b). (b) Horizontal linescans of $\mu_{S,eff}$ of the uncovered Fe/6 ML Co/Cu(001) layer (open symbols) and of ≈ 2.1 ML Ni/Fe/6 ML Co/Cu(001) (solid symbols) at the positions indicated in panel (a). The linescans result from a seven-pixel vertical average across the width of the rectangles shown in (a).

contrast, is due to a domain in the Fe/Co film with a different component of magnetization in the detection direction, as will be seen from the Co asymmetry image.

Fig. 3b shows horizontal linescans of the Fe effective spin moment for the uncovered Fe/Co/Cu(001) layer (open symbols) and centered around

2.1 ML Ni/Fe/Co/Cu(001) (solid symbols), averaged over seven vertical pixels. The linescans are done in the regions indicated in Fig. 3a by white rectangles (solid lines). In phase I for Fe thicknesses below 2 ML moments of 2.5 μ_B are observed for both films with and without Ni overlayer. Between 2 and 3 ML, already a certain reduction of the spin

moment to ≈ 2.2 μ_B is present. Between 3 and 4.5 ML the moments drop strongly. Values of 0.7 μ_B are reached without a Ni cap layer between 4.5 and 8 ML (phase II). The main difference between the linescan of the uncapped Fe/Co film and the Ni/Fe/Co film is observed around 5.5 ML Fe thickness, which we will call phase IIa in the following. Underneath the Ni layer, a value of only 0.25 μ_B is found in that region, compared to 0.7 μ_B in the uncapped Fe film. The latter value is the same as that encountered in Ni/Fe/Co for slightly higher Fe thicknesses between 6 and 8 ML (phase IIb). For thicker Fe films, the moments eventually increase to reach a value of 2.0 μ_B in phase III at around 12 ML Fe thickness.

To see the coupling behavior between the Co and Ni layers across the Fe film, images at the Co and Ni L_3 peak maximum as well as for 6-eV lower photon energy were acquired for both helicities, and normalized to the integral photon flux. From that the asymmetry of the L_3 peak heights for opposite helicity $I(\sigma_+)$ and $I(\sigma_-)$ is formed as $(I(\sigma_+) - I(\sigma_-))/(I(\sigma_+) + I(\sigma_-))$. $I(\sigma_+)$ and $I(\sigma_-)$ are thereby calculated from the difference between peak and pre-edge intensities. The resulting asymmetries at the Co and Ni edges are shown in Fig. 4. The Co layer (Fig. 4a) shows a uniform magnetization over nearly the entire range of the image. Towards higher Fe thicknesses a higher noise and maybe also a slight increase of the Co asymmetry are observed. The latter, however, could be an artifact introduced by the increasing influence of Fe absorption background at the energy of the Co L_3 absorption. Microspectroscopy measurements of Co $L_{2,3}$ absorption spectra at a different position of the same film, where the same asymmetry was found, gave a Co effective spin moment of 1.6 μ_B, and an orbital moment of 0.13 μ_B. We conclude from the similarity to the Co bulk magnetic moment that the Co film over most of the imaged area is in a saturated single domain state with the magnetization along [110]. Only in the upper right corner is a reduced asymmetry of roughly 1/2 compared to the rest of the image observed. Here the Co film is obviously not saturated. This is reflected also in the plot of the Fe spin moment (Fig. 3a), as already mentioned. It can be explained by a domain with a different magnetization direction, for example along [010], which means a projection onto the light propagation direction of $\cos(18° + 45°)$ instead of

$\cos 18°$. The presence of very small domains that are not resolved here can also not be ruled out. In any case, a macroscopic structural peculiarity of the substrate at that position, as for example locally higher roughness or higher step density, is probably the cause for the lower asymmetry. We will restrict ourselves in the following on the results from the area in which the Co film is a single domain.

Fig. 4b shows the dichroic asymmetry at the Ni L_3 edge. Pay attention to the grayscale, which is symmetric around zero in contrast to Fig. 4a. A negative Ni L_3 asymmetry of -0.09 is present around 5.5 ML Fe thickness and >3 ML Ni thickness, whereas the rest of the Ni film shows an almost constant positive value of $+0.09$. Bright contrast consequently indicates a magnetization direction parallel to that of the Co magnetization, dark contrast a magnetization direction opposite to that of the Co magnetization. Comparison of Figs. 4b and 3a reveals that the region of reversed Ni magnetization coincides exactly with the region in which the low Fe spin moment (phase IIa) is observed. Clearly no differences are seen in the Co asymmetry at that position. Altogether, antiparallel alignment of the Ni and Co magnetization is found around 5.5 ML Fe thickness in Ni/Fe/Co/Cu(001), which is correlated with an additional reduction of the apparent Fe spin moment.

The orbital moment μ_L is the second quantity that can be extracted from the pixel-by-pixel sum-rule analysis. It is found that the general behavior of μ_L is quite similar to that of the effective spin moment $\mu_{S,eff}$. It is therefore more interesting to see the behavior of the ratio of μ_L and $\mu_{S,eff}$. This is presented in Fig. 5a in a grayscale plot of the same sample area as before. Especially in the regions of low magnetic moment, the noise in $\mu_L/\mu_{S,eff}$ is rather high. In Fig. 5b linescans of the ratio of orbital to spin moment as a function of Fe thickness for 0 and 2.1 ML Ni overlayer are shown, obtained at the same positions in an identical way as the linescans shown in Fig. 3b (white rectangles in Fig. 5a). The values for $\mu_L/\mu_{S,eff}$ are mostly between 0.05 and 0.10 for both Fe/Co/Cu(001) and ≈ 2.1 ML Ni/Fe/Co/Cu(001). Between 4 and 7 ML Fe, the statistical error is too high to state a clear trend, especially when there is Ni on top of the film. A decrease of the orbital moment when reducing the Fe thickness below 2 ML is seen from Fig. 5b. Though not so
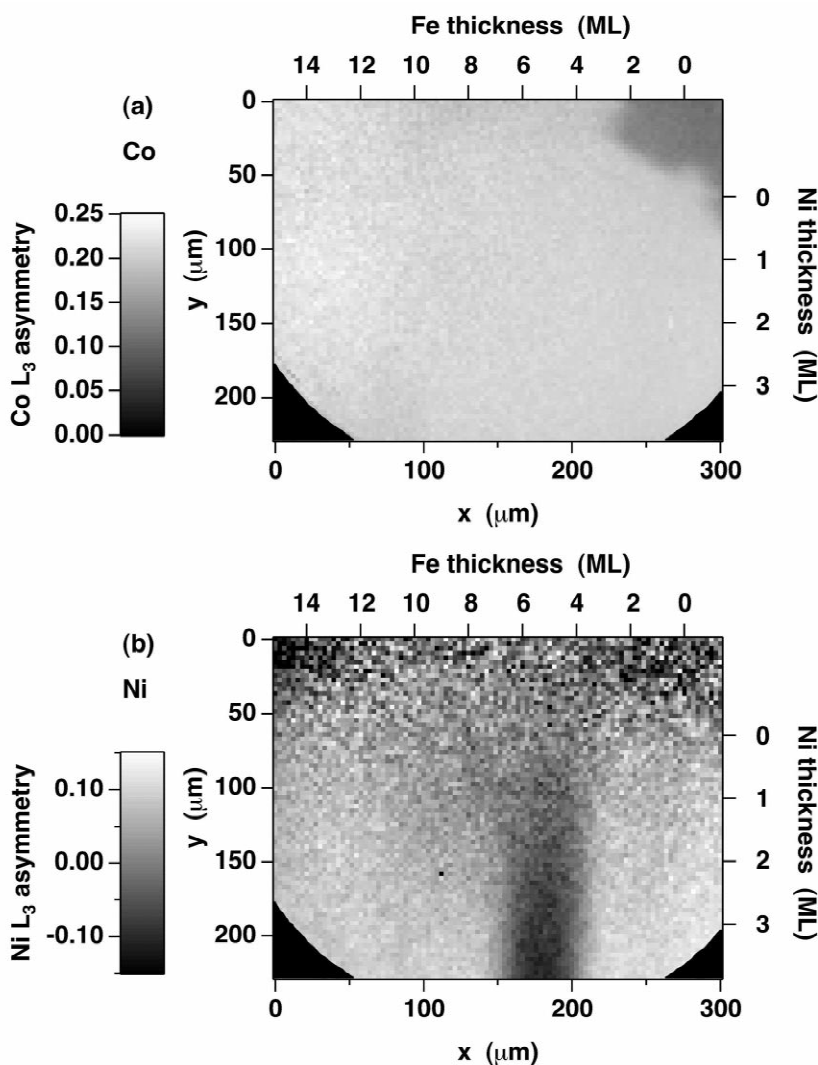
Fig. 4. (a) Co L_3 absorption asymmetry image of the difference between peak and pre-edge intensities for opposite helicities. Different levels of gray correspond to different values of the asymmetry, as explained in the legend. The imaged area is the same as in Fig. 3a. (b) Ni L_3 absorption asymmetry image. Different levels of gray correspond to different values of the asymmetry, as explained in the legend. Note that here, in contrast to panel (a), the grayscale is symmetric around zero. Around the x coordinate 180 μm, the Ni magnetization is antiparallel to the Co magnetization.

significant, another reduction of $\mu_L/\mu_{S,eff}$ may be present for increasing the Fe film thickness above 10 ML.

5. Discussion

The Fe effective spin magnetic moments observed here for uncovered Fe/Co/Cu(001) agree qualita-

tively well with those found by Schmitz et al. (3.0 μ_B in phase I, 1.1 μ_B in phase II) [43], although our values are systematically lower. The value of 0.7 μ_B at 8 ML Fe thickness (region II) contrasts the result of Refs. [39,40], where a drop in the dichroism by a factor of about ten between phase I and phase II was observed. The spin moment of 0.7 μ_B has to be interpreted as the depth-weighted average of all Fe layers. We assume here a probing depth of 17 Å [59]
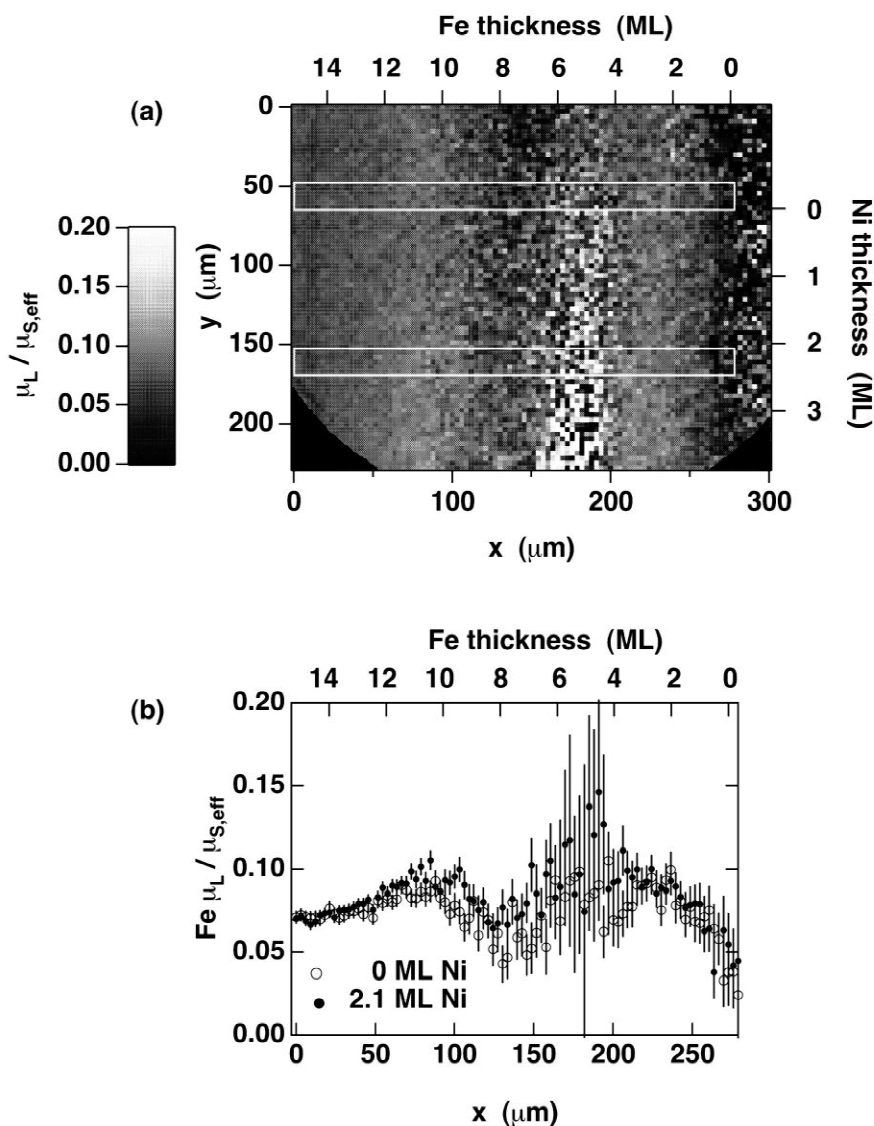
Fig. 5. (a) Result of the pixel-by-pixel sum-rule analysis for the ratio of Fe orbital to effective spin moment $\mu_L/\mu_{S,eff}$. Different levels of gray correspond to different values of $\mu_L/\mu_{S,eff}$, as explained in the legend. The white rectangles indicate the positions at which linescans are presented in panel (b). (b) Horizontal linescans of $\mu_L/\mu_{S,eff}$ of the uncovered Fe/6 ML Co/Cu(001) layer (open symbols) and of ≈ 2.1 ML Ni/Fe/6 ML Co/Cu(001) (solid symbols) at the positions indicated in panel (a). The linescans result from a seven-pixel vertical average across the width of the rectangles shown in (a).

in which the secondary electron signal is reduced by a factor of $1/e$, and an average Fe layer spacing of 1.77 Å [22,23]. A value of 0.7 μ_B would then be consistent with, for example, 2 ML ferromagnetic Fe (2.2 μ_B) on top of 6 ML non-ferromagnetic Fe, or with 1 ML ferromagnetic Fe at the surface, 5 ML

non-ferromagnetic Fe in the interior, and 2 ML ferromagnetic Fe at the Fe–Co interface. Our result thus supports the conclusion from photoelectron diffraction in magnetic dichroism of 8 ML Fe/Co/Cu(001) [45] and spin-resolved valence band photoemission [46] that ferromagnetism is present at the

surface of Fe/Co/Cu(001). It has to be noted though that a constant amount of ferromagnetic Fe at both interfaces plus non-ferromagnetic Fe in between would lead to a decreasing apparent magnetic moment with increasing Fe film thickness. This is obviously not what we observe here (cf. Fig. 3b). The situation is therefore probably more complicated. There exist several theoretical studies about the magnetic structure of fcc Fe on Cu(001) [61–68] or on Co(001) [69] which result in a layered antiferromagnetic arrangement of either monoatomic or biatomic Fe layers of different moments. The actual magnetic configuration depends sensitively on the Fe film thickness. In a real system consequently the influence of surface and interface roughness can not be neglected, and the magnetic structure of the Fe films in phase II is probably not just described in terms of magnetic and non-magnetic Fe layers. We will come back to that point later when we discuss the coupling behavior across the Fe films in phase II.

The value of 2.0 μ_B for the spin moment of bcc Fe is slightly lower than the expected Fe bulk moment of 2.2 μ_B [70], but it agrees well with XMCD measurements of thicker bcc Fe films [2]. Hunter Dunn et al. obtained values of 3.4 and 2.25 μ_B for Fe/Cu(001) in region I and III, respectively, using XMCD [14]. We believe that the discrepancy between our values of Fe/Co/Cu(001) and their values for Fe/Cu(001) could be again mainly explained by systematic errors in the sum-rule analysis, and may not be significant enough to conclude a different magnetic behavior of Fe related to the presence of the Co layer. In Ref. [43], in contrast, the Fe spin moment was even found to be about 0.2–0.3 μ_B lower in Fe/Cu(001) compared to Fe/Co/Cu(001).

An important issue for measurements of the absorption by total or partial electron yield is saturation effects [15,57–59]. Saturation effects arise when the penetration depth of the X-rays in the film for a given angle of incidence becomes comparable to the electron escape depth. They can be especially serious for Fe because of the high absorption at the Fe L_3 edge. The X-ray penetration depth, which is several thousands of Å below the Fe $L_{2,3}$ edge, is reduced to the order of only 100 Å at the L_3 absorption maximum [59]. These effects can normally only be accounted for if a series of measurements for varying angle of incidence is performed. Nakajima et al.

extracted quantitative information from comparison of absorption measurements carried out in transmission, and absorption measurements using the total electron yield [59]. From the information given in Ref. [59] we can judge the influence of saturation effects on the present measurements. Whereas for very thin Fe films no saturation effects occur, at 14 ML Fe they can result in an underestimation of the effective spin moment of about 8%, and of the orbital moment of up to 50%. Thus in Fig. 6, a tentative correction of the linescan data of Fig. 5b is shown, where the correction factor varied linearly from one at 0 ML Fe to two at 14 ML Fe. The most prominent difference with respect to Fig. 5b is consequently seen at Fe thicknesses above 8 ML. Considering the error bars in Figs. 5b and 6, the numbers derived here for the ratio of orbital to spin moment are in agreement with those of Ref. [43] for Fe/Co/Cu(001) (0.06 and 0.07 in phases I and II, respectively), and with those of Ref. [14] for Fe/Cu(001) (0.07 in phases I and III). In thicker Fe films, however, a value of only 0.043 has been measured in transmission [2].

A somewhat surprising result is the decreasing trend of the orbital moment for the very thin Fe
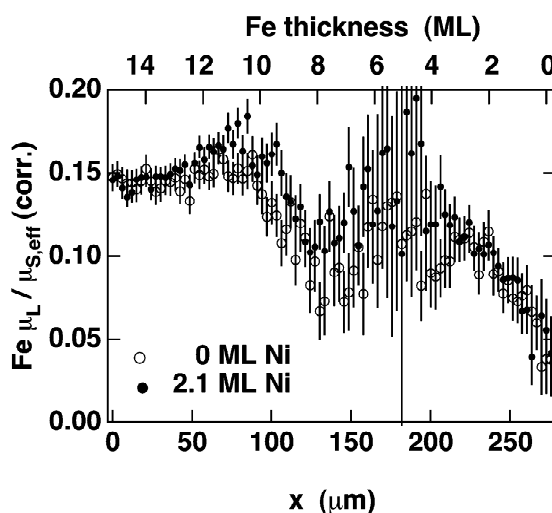

Fig. 6. Horizontal linescans of Fe $\mu_L/\mu_{S,eff}$ of the uncovered Fe/6 ML Co/Cu(001) layer (open symbols) and of ≈ 2.1 ML Ni/Fe/6 ML Co/Cu(001) (solid symbols) like in Fig. 5b, corrected for saturation effects. A factor that varied linearly in Fe thickness from one at 0 ML Fe to two at 14 ML Fe was assumed for the correction.

films. Usually it is assumed that a reduction of atomic coordination and dimensionality in the sub-monolayer thickness range leads to an increasing orbital contribution to the magnetic moment [71,72]. Such a tendency has been observed experimentally for decreasing thickness of Co films on Cu(001) [73] and Fe atomic monolayers in $L1_0$ FeCu layered compounds [50,51]. The answer for the opposite thickness behavior of the Fe orbital moment in Fe/Co/Cu(001) may be found in the details of the hybridization between Fe and Co electronic states. Theoretical calculations could help to check for such an influence of the Co underlayer on the Fe orbital moment. Another point that should be considered in the discussion of orbital moments is the connection to magnetic anisotropy. In a simple perturbation model the anisotropy of the orbital moment is linked to the magnetocrystalline anisotropy [74]. This leads to higher orbital moments in samples magnetized along the preferred magnetization axis compared to a magnetization direction along a hard axis [49,52,53,75–78]. For increased strength of the anisotropy, the orbital moment difference between measurements with saturation along the easy and hard axes is increased in a way that the hard axis orbital moment is reduced, and the easy axis orbital moment enhanced [52,53,78].

Fe films on Cu(001) show a perpendicular aniso-tropy in the thickness range 0–11 ML [29–32]. From the structural similarity of Fe/Cu(001) and Fe/Co/Cu(001) [39–42] it would be plausible that the intrinsic spin–orbit-derived anisotropy of Fe in Fe/Co/Cu(001) is also perpendicular, and that it is the in-plane anisotropy contribution of the Co layer that forces the Fe/Co bilayer magnetization into the film plane. A higher perpendicular magnetocrystalline anisotropy of the thinner Fe film would thus be correlated with a lower orbital moment, measured in the in-plane magnetized Fe/Co film. This could be a reason for the observed reduction of the Fe orbital moment at very low Fe thicknesses (cf. Fig. 6). Following Ref. [74] there should be a linear relation-ship between the magnetocrystalline anisotropy and the orbital moment difference, with the propor-tionality constant being the spin–orbit coupling parameter times a prefactor that depends on the band structure. This factor should be between 2.5 and 5 meV/μ_B for 3d transition metals [52,53]. Experimen-

tally, for Co/Au a factor as low as 0.8 meV/μ_B was found [78], whereas a factor of roughly 4 meV/μ_B could explain observations made in Ni films [49]. The thickness dependence of the magnetocrystalline anisotropy of Fe/Cu(001) follows approximately a 240 μeV/t + const. behavior [31,32], where t is the Fe thickness in ML. This converts into an estimate of the expected Fe orbital moment anisotropy of rough-ly 0.05 μ_B /t + const., or 0.02$\mu_{S,eff}$ /t + const., with $\mu_{S,eff} = 2.5$ μ_B. The observed reduction of the orbital moment at low Fe thicknesses is thus of the same order of magnitude as the expected influence of the magnetocrystalline anisotropy. The enhancement at Fe thicknesses above 10 ML could be analogously explained by the lower perpendicular anisotropy in phase III [32].

We now turn our attention to the antiferromagnetic alignment of the Ni layer with respect to the Co layer around 5.5 ML Fe thickness (Fig. 4), and its influence on the Fe spin moment (Fig. 3). If we assume ferromagnetic Fe layers at both interfaces, then these layers would experience a strong direct ferromagnetic coupling to the respective neighboring magnetic layers (Co or Ni). In the case of anti-ferromagnetic alignment of Co and Ni, the Fe layers at both interfaces should consequently be aligned oppositely to each other. This leads to a lower apparent moment compared to a ferromagnetic align-ment. The small positive net Fe moment seen experimentally in that case (≈ 0.25 μ_B) could thus be due to the (incomplete) cancellation of these interface contributions. As a model, a 5 ML Fe film composed of two ferromagnetic layers at the Fe–Co interface, two non-ferromagnetic layers above, and one oppositely magnetized atomic layer at the Ni–Fe interface will provide about 0.2 μ_B when measured by XMCD. This is close to the experimental value. It could, however, also be explained by a model in which just the interface layer at the Co–Fe interface contributes to ferromagnetism.

The question remains why a higher moment is observed in the uncovered Fe/Co film around 5.5 ML Fe thickness. One could think of relating this to ferromagnetic contributions from Fe interface layers from both interfaces as in the case of Ni/Fe/Co, but this time aligned parallel. Quantitatively, however, this does not give exactly the experimental observa-tion. Assuming the same model as before but with a

parallel alignment of all contributing layers (i.e., one Fe layer at the Fe–Ni interface and two Fe layers at the Co–Fe interface being ferromagnetic with the magnetization pointing all in the same direction) a value of 1.3 μ_B is expected by XMCD. This is about a factor of two higher than what is observed. The reason for the different Fe moment with and without the Ni overlayer can thus not just be the presence and absence of antiferromagnetic alignment of magnetic Fe interface layers within the Fe film. As mentioned before, the very simple model where we assume ferromagnetic and non-ferromagnetic layers does not adequately describe the thickness dependence of the Fe spin moment in phase II. Although the value of 0.7 μ_B at 8 ML is a clear hint for a ferromagnetic surface layer magnetically aligned with the Co film, a much higher value would be expected at 5 ML, where the contribution of the non-ferromagnetic layers is relatively decreased. It is thus feasible that there is a partial antiferromagnetic alignment of the Fe surface with respect to the Co at the uncapped 5 ML Fe/Co film. The experimental observations could be explained as the result of the influence of interface roughness and magnetic frustrations with and without Ni overlayer. A more realistic model with layerwise or bilayerwise antiferromagnetism will have to be taken into account. There is also the possibility that without Ni a 90° orientation of the magnetization of the Fe surface layer around 5 ML Fe thickness is present after the application of the external field, similar to the 'spin-flop' state in antiferromagnets. One has also to consider the presence of non-collinear moments induced by frustrations at step edges, as proposed by Lorenz and Hafner [66], which might further complicate the interpretation, or the existence of a non-collinear spin-spiral phase in the Fe layer [67,68].

In (001)-oriented Fe/$Ni_{81}Fe_{19}$ multilayers, antiferromagnetic coupling between the $Ni_{81}Fe_{19}$ layers has been observed around 9 Å Fe layer thickness [47]. This Fe layer thickness coincides quite well with the thickness of 5.5 ML, at which we observe the antiferromagnetic coupling between the Ni and Co films. Escorcia-Aparicio et al. concluded from a magneto-optical Kerr-effect study of Co/Fe/Co/Cu(001) that antiferromagnetic coupling between the two Co layers is present in the entire thickness range of phase II, namely from 7.4 to 16.4 Å [41,42]. They

distinguished between 'weak' and 'strong' antiferromagnetic coupling. Whereas split hysteresis loops were observed in the former regime, no saturation was possible in fields up to 1.9 kOe in the latter regime [41,42]. 'Strong' antiferromagnetism was found around 7 Å Fe thickness. This corresponds to slightly less than 4 ML, and is thus somewhat lower than the value we find in the Ni/Fe/Co trilayers. We nevertheless think that it is the same underlying mechanism that is responsible for both. Having Ni instead of Co as one of the sandwiching layers could account for the difference in Fe film thickness for the antiferromagnetic interlayer coupling.

In contrast to Refs. [41,42] we do not observe antiferromagnetic coupling other than around 5.5 ML Fe thickness. In studies of interlayer exchange coupling [79] it was never observed that antiferromagnetic coupling occurred over an extended thickness range as it was claimed for the 'weak' antiferromagnetic coupling in Co/Fe/Co in Refs. [41,42]. We therefore believe that the split magnetization loops in phase II of Refs. [41,42] have other reasons. It is conceivable that the influence of step-induced uniaxial in-plane anisotropies becomes dominant in the case of small (ferromagnetic) interlayer coupling, leading to a two-step magnetization reversal process with reduced remanence. Another explanation could be a biquadratic (90°) coupling of the two Co layers caused by a higher substrate roughness than in our case. In that case, though, one would expect to observe also a region of ferromagnetic coupling, since biquadratic coupling is thought to be the consequence of competing ferromagnetic and antiferromagnetic contributions mixed by film morphology [80,81].

In Refs. [41,42] two different regions of 'strong' antiferromagnetic coupling have been observed, which could suggest some kind of oscillatory exchange coupling across the Fe layer. The second region of 'strong' antiferromagnetic coupling was found just at the Fe thicknesses where the films convert to bcc Fe (phase III), and thus was obscured by the reappearance of ferromagnetism. To test that point, the authors of Refs. [41,42] grew also a Co/Fe/Co trilayer on a deliberately contaminated Cu(001) substrate. It is known that carbon can extend the thickness range of phase II in Fe/Cu(001) [33–35]. A more pronounced region of 'strong'

antiferromagnetic coupling was then found in such films at around 18 Å Fe thickness [41,42]. In our films, we conclude from the behavior of the spin moment as a function of Fe thickness that the conversion of fcc to bcc Fe is getting significant already at 9–10 ML Fe thickness (cf. Fig. 3b). This is consistent with the observation from scanning tunnelling microscopy that small amounts of bcc precipitates in Fe/Cu(001) are present already at Fe thicknesses as low as 6 ML [27]. The complete absence of a second region of antiferromagnetic coupling in our Ni/Fe/Co films could thus just be the consequence of the occurrence of the bcc Fe phase, which gives rise to a direct strong ferromagnetic coupling between the Ni and Co layers.

Such a second region of possible antiferromagnetic coupling was indeed observed in a preliminary experiment on Ni/Fe/Co/Cu(001) that was carried out shortly after a bake-out of the chamber. Here the pressure during Fe evaporation rose to 2×10^{-7} Pa. The result is presented in Fig. 7. It shows, from left to right, the Co, Fe, and Ni L_3 asymmetry images of a crossed double wedge similar to the double wedge described above. Different shades of gray correspond to different (positive and negative) values of the asymmetry, as explained in the legend. The Fe and Ni thicknesses are given at the upper and right axes, respectively. Horizontal linescans of the asymmetry, taken at 4 ± 0.5 ML Ni thickness, are shown superimposed over the images. In the upper right corner of the images a region with incomplete or rotated magnetization can be recognized, which we ignore in the following. Comparing the Fe image of Fig. 7 to Fig. 3a, one can see that in the 'dirty' film the onset
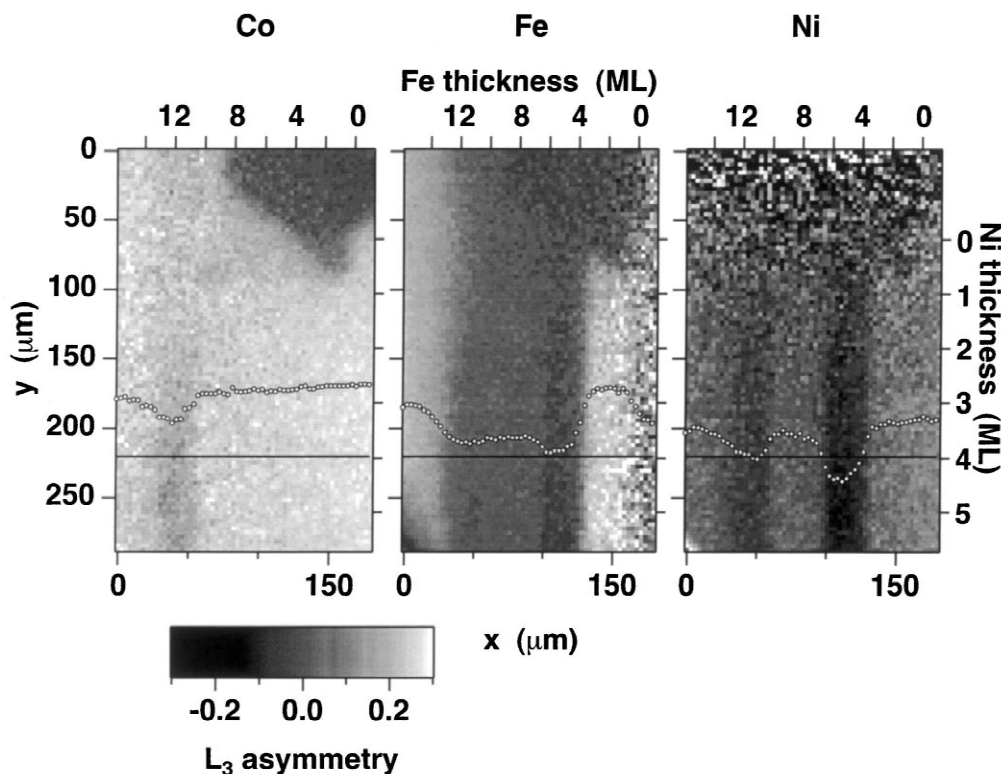

Fig. 7. Co, Fe, and Ni (from left to right) L_3 absorption asymmetry images of a crossed double wedge similar to the one shown in Figs. 3–5, but prepared under worse vacuum conditions (pressure during Fe evaporation $\approx 2 \times 10^{-7}$ Pa). Different shades of gray correspond to different (positive or negative) values of the asymmetry, as explained in the legend. The Fe and Ni thicknesses are given at the upper and right axes, respectively. Two distinct stripes of darker contrast are observed in the Fe and Ni asymmetry images at about 5 and 11 ML Fe thickness. Linescans of the asymmetry, taken at 4 ± 0.5 ML Ni thickness as 14-pixel vertical average, are shown superimposed.

of the bcc phase, characterized by the bright contrast, is located at 12–13 ML Fe thickness, about 1–2 ML higher thickness than in the clean film of Fig. 3a (11 ML). At 5.5 ML Fe, basically the same behavior as in the clean film is observed. At that Fe thickness the Ni magnetization is oriented antiparallel to the Co film, and the Fe asymmetry exhibits a distinctly lower asymmetry at the same position. The difference of the 'dirty' film with respect to the clean film is the observation of a second dark stripe in both the Fe and Ni asymmetry images at around 11 ML Fe thickness. Also in the Co image a slightly lower asymmetry is seen at that position. This second dark stripe could be a hint towards a second oscillation of antiferromagnetic interlayer coupling. The difference in thickness between the first and second region is about 6 ML (≈ 11 Å). This is the same as found between the regions of 'strong' antiferromagnetic coupling in Refs. [41,42], and also similar to the long period oscillations in most fcc transition metal systems [79]. Unlike the first dark stripe at 5.5 ML Fe thickness, however, the second stripe at 11 ML does not show negative asymmetry at the Ni L_3 edge, but just a value close to zero. This could of course be a consequence of the smaller coupling strength in the second antiferromagnetic maximum. Nevertheless, the present images do not strictly prove antiferromagnetic coupling in that region. Another explanation could, for example, be a greatly enhanced coercivity due to structural imperfections in the transition region from fcc to bcc. A non-collinear arrangement of Fe moments at that thickness, induced by an enhanced step density, could also be a possibility. On the other hand, the dark contrast in the Co image of Fig. 7 is not explained by just an enhanced coercivity in the Fe film, since the sample was already magnetized a first time after deposition of the Co layer. Altogether, we think that the present data show indications suggesting oscillatory exchange coupling through the Fe layer in the system Ni/Fe/Co/Cu(001).

6. Conclusions

We have used the combination of PEEM and XMCD spectroscopy in a study of the magnetic phases of Fe in Fe/Co/Cu(001) and Ni/Fe/Co/Cu(001). This full-image microspectroscopic technique allows spectroscopic information to be obtained on a microscopic scale. It can be used to image element-resolved quantitative magnetic properties. Microspectroscopy of crossed double wedges greatly facilitates the magnetic characterization of layered systems, as shown in the present case.

The magnetic phases of Fe on Co/Cu(001) have been identified, and their magnetic properties (effective spin moment, orbital moment) could be determined simultaneously for any position in the double wedge. Below 4 ML Fe, a high moment ferromagnetic phase is found. The reduced net magnetic moment between 4 and ≈ 10 ML Fe thickness is due to a complicated non-ferromagnetic configuration of fcc Fe. From the size of the experimentally measured spin moment we conclude that at 7–9 ML Fe thickness, the Fe surface layer contributes to the ferromagnetic signal of the film. The antiparallel orientation of the Ni magnetization in Ni/5.5 ML Fe/Co/Cu(001) is most likely due to antiferromagnetic coupling across the Fe layer at that thickness. It is not entirely clear what happens without Ni layer at 5.5 ML Fe/Co/Cu(001). The observed net magnetization of the Fe layer at that thickness is probably also affected by antiferromagnetic coupling between the Co film and the Fe surface layer. Above ≈ 10 ML Fe thickness, the films are again ferromagnetic in both the Ni/Fe/Co and the Fe/Co systems, with a somewhat lower moment than in phase I. The Fe orbital to effective spin moment ratio does not show a distinctly different behavior in the three phases. We interpret the decrease towards small Fe thicknesses as an influence of Fe magnetocrystalline anisotropy on the orbital moment. Images taken from Ni/Fe/Co/Cu(001) trilayers prepared under enhanced residual gas supply indicate that the magnetic coupling across the phase II Fe film might be due to an oscillatory interlayer coupling. In addition to 5.5 ML Fe thickness, in these images, reduced Ni and Fe apparent moments were also observed around 11 ML Fe thickness, that is, at about 6 ML higher Fe thickness. This could be the signature of a second antiferromagnetic maximum. Detailed field-dependent studies should help to clarify the coupling behavior across fcc Fe, and to deduce quantitative information about the coupling strength.

Acknowledgements

References

[1] G. Schütz, W. Wagner, W. Wilhelm, P. Kienle, R. Zeller, R. Frahm et al., Phys. Rev. Lett. 58 (1987) 737.

[2] C.T. Chen, Y.U. Idzerda, H.-J. Lin, N.V. Smith, G. Meigs, E. Chaban et al., Phys. Rev. Lett. 75 (1995) 152.

[3] J. Stöhr, J. Electron Spectrosc. Relat. Phenom. 75 (1995) 253.

[4] J.L. Erskine, E.A. Stern, Phys. Rev. B 12 (1975) 5016.

[5] B.T. Thole, P. Carra, F. Sette, G. van der Laan, Phys. Rev. Lett. 68 (1992) 1943.

[6] P. Carra, B.T. Thole, M. Altarelli, X. Wang, Phys. Rev. Lett. 70 (1993) 694.

[7] R. Wu, A.J. Freeman, Phys. Rev. Lett. 73 (1994) 1994.

[8] W.L. O'Brien, B.P. Tonner, G.R. Harp, S.S.P. Parkin, J. Appl. Phys. 76 (1994) 6462.

[9] D. Rioux, B. Allen, H. Höchst, D. Zhao, D.L. Huber, Phys. Rev. B 56 (1997) 753.

[10] Y.U. Idzerda, C.T. Chen, H.-J. Lin, H. Tjeng, G. Meigs, Physica B 208–209 (1995) 746.

[11] Y. Teramura, A. Tanaka, T. Jo, J. Phys. Soc. Jpn. 65 (1996) 1053.

[12] J. Vogel, M. Sacchi, Phys. Rev. B 49 (1994) 3230.

[13] X. Le Cann, C. Boeglin, B. Carrière, K. Hricovini, Phys. Rev. B 54 (1996) 373.

[14] J. Hunter Dunn, D. Arvanitis, N. Mårtensson, Phys. Rev. B 54 (1996) R11157.

[15] V. Chakarian, Y.U. Idzerda, C.T. Chen, Phys. Rev. B 57 (1998) 5312.

[16] J. Stöhr, Y. Wu, M.G. Samant, B.B. Hermsmeier, G. Harp, S. Koranda et al., Science 259 (1993) 658.

[17] W. Kuch, R. Frömter, J. Gilles, D. Hartmann, Ch. Ziethen, C.M. Schneider et al., Surf. Rev. Lett. 5 (1998) 1241.

[18] W. Swiech, G.H. Fecher, Ch. Ziethen, O. Schmidt, G. Schönhense, K. Grzelakowski et al., J. Electron Spectrosc. Relat. Phenom. 84 (1997) 171.

[19] C.M. Schneider, J. Magn. Magn. Mater. 175 (1997) 160.

[20] M.T. Kief, W.F. Egelhoff Jr., Phys. Rev. B 47 (1993) 10785.

[21] K. Heinz, S. Müller, P. Bayer, Surf. Sci. 337 (1995) 215.

[22] P. Bayer, S. Müller, P. Schmailzl, K. Heinz, Phys. Rev. B 48 (1993) 17611.

[23] S. Müller, P. Bayer, A. Kinne, P. Schmailzl, K. Heinz, Surf. Sci. 322 (1995) 21.

[24] D. Li, M. Freitag, J. Pearson, Z.Q. Qiu, S.D. Bader, Phys. Rev. Lett. 72 (1994) 3112.

[25] M. Straub, R. Vollmer, J. Kirschner, Phys. Rev. B 77 (1996) 743.

[26] M. Wuttig, B. Feldmann, J. Thomassen, F. May, H. Zillgen, A. Brodde et al., Surf. Sci. 291 (1993) 14.

[27] J. Giergiel, J. Kirschner, J. Landgraf, J. Shen, J. Woltersdorf, Surf. Sci. 310 (1994) 1.

[28] J. Giergiel, J. Shen, J. Woltersdorf, A. Kirilyuk, J. Kirschner, Phys. Rev. B 52 (1995) 8528.

[29] J. Thomassen, F. May, B. Feldmann, M. Wuttig, H. Ibach, Phys. Rev. Lett. 69 (1992) 3831.

[30] P. Xhonneux, E. Courtens, Phys. Rev. B 46 (1992) 556.

[31] D.E. Fowler, J.V. Barth, Phys. Rev. B 53 (1996) 5563.

[32] W. Platow, A.N. Anisimov, M. Farle, K. Baberschke, Phys. Stat. Sol. (a) 173 (1999) 145.

[33] S.D. Bader, J. Appl. Phys. 76 (1994) 6425.

[34] A. Kirilyuk, J. Giergiel, J. Shen, J. Kirschner, Phys. Rev. B 52 (1995) R11672.

[35] A. Kirilyuk, J. Giergiel, J. Shen, M. Straub, J. Kirschner, Phys. Rev. B 54 (1996) 1050.

[36] M. Zharnikov, A. Dittschar, W. Kuch, C.M. Schneider, J. Kirschner, Phys. Rev. Lett. 76 (1996) 4620.

[37] M. Zharnikov, A. Dittschar, W. Kuch, C.M. Schneider, J. Kirschner, J. Magn. Magn. Mater. 174 (1997) 40.

[38] R. Vollmer, J. Kirschner, Phys. Rev. B 61 (2000) 4146.

[39] W.L. O'Brien, B.P. Tonner, Surf. Sci. 334 (1995) 10.

[40] W.L. O'Brien, B.P. Tonner, Phys. Rev. B 52 (1995) 15332.

[41] E.J. Escorcia-Aparicio, R.K. Kawakami, Z.Q. Qiu, Phys. Rev. B 54 (1996) 4155.

[42] R.K. Kawakami, E.J. Escorcia-Aparicio, Z.Q. Qiu, J. Appl. Phys. 79 (1996) 4532.

[43] D. Schmitz, C. Charton, A. Scholl, C. Carbone, W. Eberhardt, Phys. Rev. B 59 (1999) 4327.

[44] W. Kuch, J. Gilles, S.S. Kang, F. Offi, J. Kirschner, S. Imada, S. Suga, J. Appl. Phys. 87 (2000) 5747.

[45] X. Gao, M. Salvietti, W. Kuch, C.M. Schneider, J. Kirschner, Phys. Rev. B 58 (1998) 15426.

[46] R. Kläsges, D. Schmitz, C. Carbone, W. Eberhardt, T. Kachel, Solid State Commun. 107 (1998) 13.

[47] W. Kuch, S.S.P. Parkin, J. Magn. Magn. Mater. 184 (1998) 127.

[48] Y. Saitoh, T. Nakatani, T. Matsushita, T. Miyahara, M. Fujisawa, K. Soda et al., J. Synchrotron Rad. 5 (1998) 542.

[49] W. Kuch, J. Gilles, S.S. Kang, S. Imada, S. Suga, J. Kirschner, Phys. Rev. B (2000), in press.

[50] W. Kuch, M. Salvietti, X. Gao, M.-T. Lin, M. Klaua, J. Barthel et al., Phys. Rev. B 58 (1998) 8556.

[51] W. Kuch, M. Salvietti, X. Gao, M. Klaua, J. Barthel, C.V. Mohan et al., J. Appl. Phys. 83 (1998) 7019.

[52] D. Weller, J. Stöhr, R. Nakajima, A. Carl, M.G. Samant, C. Chappert et al., Phys. Rev. Lett. 75 (1995) 3752.

[53] H.A. Dürr, G. van der Laan, B.T. Thole, Phys. Rev. Lett. 76 (1996) 3464.

[54] C.F.J. Flipse, J.J. de Vries, G. van der Laan, M. Surman, A. Partridge et al., J. Magn. Magn. Mater. 148 (1995) 141.

[55] H.A. Dürr, G. van der Laan, Phys. Rev. B 54 (1996) R760.

[56] G. van der Laan, H.A. Dürr, Physica B 248 (1998) 121.

[57] W.L. O'Brien, B.P. Tonner, Phys. Rev. B 50 (1994) 2963.

[58] J. Hunter Dunn, D. Arvanitis, N. Mårtensson, M. Tischer, F. May, M. Russo et al., J. Phys.: Cond. Matt. 7 (1995) 1111.

[59] R. Nakajima, J. Stöhr, Y.U. Idzerda, Phys. Rev. B 59 (1999) 6421.

[60] S. Imada, T. Muro, T. Shishidou, S. Suga, H. Maruyama, K. Kobayashi et al., Phys. Rev. B 59 (1999) 8752.

[61] R. Lorenz, J. Hafner, Phys. Rev. B 54 (1996) 15937.

[62] L. Szunyogh, B. Újfalussy, P. Weinberger, Phys. Rev. B 55 (1997) 14392.

[63] T. Asada, S. Blügel, Phys. Rev. Lett. 79 (1997) 507.

[64] T. Asada, S. Blügel, J. Magn. Magn. Mater. 177–181 (1998) 1233.

[65] Y. Zhou, W. Zhang, L. Zhong, X. Nie, D.-S. Wang, J. Magn. Magn. Mater. 167 (1997) 136.

[66] R. Lorenz, J. Hafner, Phys. Rev. B 58 (1998) 5197.

[67] M. Uhl, L.M. Sandratski, J. Kübler, Phys. Rev. B 50 (1994) 291.

[68] P.M. Marcus, S.L. Qiu, V.L. Moruzzi, J. Phys. Cond. Matt. 11 (1999) 5709.

[69] A. Mokrani, O. Elmouhssine, G. Moraïtis, C. Demangeat, J. Magn. Magn. Mater. 198–199 (1999) 561.

[70] E.P. Wohlfahrt, in: E.P. Wohlfahrt (Ed.), Ferromagnetic Materials, Vol. 1, North Holland, Amsterdam, 1980.

[71] O. Eriksson, L. Nordström, A. Pohl, L. Severin, A.M. Boring, B. Johansson, Phys. Rev. B 41 (1990) 11807.

[72] H. Ebert, R. Zeller, B. Drittler, P.H. Dederichs, J. Appl. Phys. 67 (1990) 4576.

[73] M. Tischer, O. Hjortstam, D. Arvanitis, J. Hunter Dunn, F. May, K. Baberschke et al., Phys. Rev. Lett. 75 (1995) 1602.

[74] P. Bruno, Phys. Rev. B 39 (1989) 865.

[75] D. Weller, Y. Wu, J. Stöhr, M.G. Samant, B.D. Hermsmeier, C. Chappert, Phys. Rev. B 49 (1994) 12888.

[76] J. Stöhr, H. König, Phys. Rev. Lett. 75 (1995) 3748.

[77] H.A. Dürr, G.Y. Guo, G. van der Laan, J. Lee, G. Lauhoff, J.A.C. Bland, Science 277 (1997) 213.

[78] J. Stöhr, J. Magn. Magn. Mater. 200 (1999) 470.

[79] B. Heinrich, J.A.C. Bland (Eds.), Ultrathin Magnetic Structures, Vol. 2, Springer, Berlin, 1994, and references therein.

[80] J. Slonczewski, Phys. Rev. Lett. 67 (1991) 3172.

[81] J. Slonczewski, J. Magn. Magn. Mater. 150 (1995) 13.